This article has been accepted for publication in a future issue of this journal, but has not been fully edited. Content may change prior to final publication. Citation information: DOI 10.1109/TMI.2017.2770147, IEEE Transactions on Medical Imaging

The Gamma Characteristic of Reconstructed PET Images: Implications for ROI Analysis.

Tian Mou, Jian Huang and Finbarr O'Sullivan

***Abstract*—The basic emission process associated with PET imaging is Poisson in nature. Reconstructed images inherit some aspects of this—regional variability is typically proportional to the regional mean. Iterative reconstruction using expectation-maximization (EM), widely used in clinical imaging now, impose positivity constraints that impact noise properties. The present work is motivated by analysis of data from a physical phantom study of a PET/CT scanner in routine clinical use. Both traditional filtered back-projection (FBP) and EM reconstructions of the images are considered. FBP images are quite Gaussian but the EM reconstructions exhibit Gamma-like skewness. The Gamma structure has implications for how reconstructed PET images might be processed statistically. Post-reconstruction inference—model fitting and diagnostics for regions of interest are of particular interest. Although the relevant Gamma parameterization is not within the framework of generalized linear models (GLM), iteratively re-weighted least squares (IRLS) techniques, which are often used to find the maximum likelihood estimates of a GLM, can be adapted for analysis in this setting. Our work highlights the use of a Gamma-based probability transform in producing normalized residuals as model diagnostics. The approach is demonstrated for quality assurance analyses associated with physical phantom studies—recovering estimates of local bias and variance characteristics in an operational scanner. Numerical simulations show that when the Gamma assumption is reasonable, gains in efficiency are obtained. The work shows that the adaptation of standard analysis methods to accommodate the Gamma structure is straightforward and beneficial.**

***Index Terms*—Image processing, Gamma distribution, IRLS, PET.**

I. INTRODUCTION

POSITRON emission tomography (PET) is widely used in the clinical management of many cancers—for staging, therapy planning and evaluation of therapy response. So improved understanding of the characteristics of PET imaging measurements could benefit clinical decision making. The analysis of statistical variation in PET images, and specifically the problem of approximating standard errors for regional means, has received considerable attention [2, 6, 7, 9, 13, 21]. Most of this work has necessarily concentrated on classical filtered-backprojection (FBP) reconstruction. With the widespread use of positivity constrained EM [23] reconstructions in clinical practice, the nature of the distribution of such reconstructions is receiving more careful attention. A basic result in probability is that sums of independent Poisson random variables are also Poisson. With PET the emission process can be viewed as a realization of a Poisson process, and so the local weighted-averaging nature of classical reconstruction kernels theoretically implies a relation between the mean and variance of reconstructed values [7, 21]. This is a familiar characteristic of the Poisson and other distributions such as the Gamma and log-normal. Many factors impact on the noise characteristics of reconstructed PET images and might lead to a deviation from the Poisson distribution: most obviously scaling but attenuation and scatter corrections add further complexities. Barret et al. [3] and Li [12] theoretically analyzed the noise properties/propagation of iterative reconstruction algorithms and suggested that the probability density function of the grey level at each pixel of the reconstructed images can be approximated by a log-normal distribution.Teymurazyan et al. [22] reported measurements on a GEMINI PET/CT scanner comparing FBP and iterative EM reconstructions. While Gaussian characteristics were reasonable for FBP reconstructed images, the EM-reconstructed images were typically skewed. Their work suggested consideration of the Gamma distribution for representation of measurements. In cases where the reconstructed images are further analyzed or quantitively interpreted, as is the case in kinetic studies, the procedures used should ideally incorporate a good understanding of the statistical characteristics of the measurements in order that they be efficient [18]. In this context least-squares (or weighted least squares), which is efficient for Gaussian data, may not be efficient/optimal for Gamma or log-normal data.

Motivated by experience with our own scanner, this work explores the Gamma model in greater detail and provides inference implications associated with such a representation of PET images. Iteratively re-weighted least squares techniques are described to implement likelihood inference based on the Gamma assumption. This makes essential use of approximations for the di-gamma and tri-gamma functions [1]. The development highlights use of the Gamma probability transform for creation of normalized residual diagnostics associated with such analyses. The methods are illustrated in the context of routine Quality Assurance (QA) studies used to evaluate the temporal and axial imaging characteristics of a scanner. Results are reported for data from 3-D imaging in an operational clinical scanner—a GE Discovery STE PET/CT.

The basic theory and methodology is developed in section II. Studies with real and simulated data are described in section III. Section IV presents data analysis for FBP and EM reconstruction images. The paper concludes with discussion including some exploration of the impact of spatial covariance

This work was supported in part by Science Foundation Ireland Grant No. PI-11/1027.

Tian Mou, Jian Huang and Finbarr O'Sullivan are with the Department of Statistics, University College Cork, Ireland (e-mail: j.huang@ucc.ie).

This article has been accepted for publication in a future issue of this journal, but has not been fully edited. Content may change prior to final publication. Citation information: DOI 10.1109/TMI.2017.2770147, IEEE Transactions on Medical Imaging

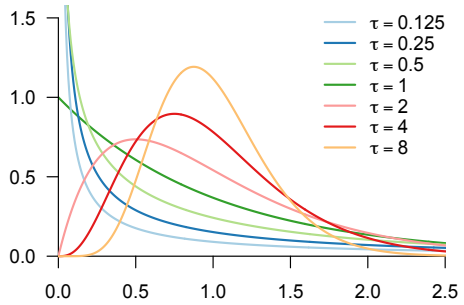

Fig. 1. Densities of $\text{Gamma}(\tau\mu, 1/\tau)$ with $\mu = 1$ for different τ-values.

on the results.

II. Methodological Development

While reconstructed PET images are not integer counts they typically inherit the mean-variance property of the Poisson distribution [6, 13, 17, 19]. Positivity constrained EM reconstructions [23] effectively replace negative values with ones that are positive—inducing some skewness. As shown in Fig. 1 the Gamma distribution, which has the flexibility to describe such data, is plausible in this setting. We use the parameterization $\text{Gamma}(\tau\frac{\mu}{\phi}, \phi)$ to represent reconstructed PET activity values. This specifies a Gamma distribution with shape parameter $\tau\frac{\mu}{\phi}$ and scale parameter ϕ, the density function is

$$f(x|\tau,\mu,\phi) = \frac{1}{\Gamma(\tau\frac{\mu}{\phi})\phi^{\frac{\tau\mu}{\phi}}} x^{\frac{\tau\mu}{\phi}-1} e^{-\frac{x}{\phi}}$$

where $\Gamma(\cdot)$ is the gamma function. Here τ corresponds to the injection dose. The mean and variance of the data will be $\tau\mu$ and $\tau\mu\phi$, respectively. The parameter ϕ represents over-dispersion relative to a Poisson random variable. In practice, such dispersion routinely arises from corrections for detector sensitivity, attenuation and scatter—but other factors such as patient movement may also play a role. Often PET measurements are scaled by the injected dose per weight of the patient for analysis, *e.g.*, converted into standardized uptake value (SUV) units [10]. If the counts are scaled by dose, they will have a $\text{Gamma}(\tau\frac{\mu}{\phi}, \frac{\phi}{\tau})$ distribution—the mean is μ and the variance is $\mu\phi/\tau$. Fig. 1 shows $\text{Gamma}(\tau\mu, 1/\tau)$ densities for different τ-values with $\mu = 1$. When $\tau \leq 1$, the Gamma distributions have an exponential-like shape. The skewness reduces and the distribution formally converges to a Gaussian as the value of τ or $\frac{\mu\tau}{\phi}$ increases.

We address inference for a certain class of important models involving both temporal and spatial features, when the data have a Gamma structure. Complexity arises because our interest is focused on the mean and variance parameter, thus, unlike the estimation problem of the Gamma distribution in generalized linear models where the dispersion parameter ϕ is a constant and considered as known/unknown nuisance parameter. As μ and ϕ are both of inferential interest, the exponential family structure and the familiar IRLS procedures, associated with the Gamma distribution in generalized linear models [14], do not apply.

A. Inference for Multiplicative Models in the Gamma Setting

Consider the situation where we have region of interest (ROI) time-course data. Hence, let z_{it}, for $t = 1, 2, ..., T$ and $i = 1, 2, ..., N$ be the set of voxel-level decay-corrected PET tracer activity values (scaled by injected dose) for a ROI with N voxels measured over T time-frames. Assuming the region is relatively homogeneous, we might reasonably expect a common temporal characteristic for the data in the ROI, *e.g.*, $z_{it} \sim \text{Gamma}(\mu_t/\phi_t, \phi_t)$ with $E(z_{it}) = \mu_t$ and $Var(z_{it}) = \phi_t\mu_t$. Assuming the duration of the t'th time-frame of scanning is Δ_t and the decay-correction factor for the t'th time-frame is f_t, then ϕ_t would be of the form $\phi\frac{f_t}{\Delta_t}$[8]. In the case that the ROI extended over several slices or there were significant changes in sensitivity due to the attenuation of radiation, the model is readily adapted to take this into account. This leads to consideration of a general structure in which $z_{ikt} \sim \text{Gamma}(\boldsymbol{\mu}_{kt}/\boldsymbol{\phi}_{kt}, \boldsymbol{\phi}_{kt})$ and

$$\boldsymbol{\mu}_{kt} = \alpha_k\mu_t \quad \text{and} \quad \boldsymbol{\phi}_{kt} = \beta_k\phi_t \tag{1}$$

where $\boldsymbol{\mu}_{kt}$ and $\boldsymbol{\phi}_{kt}$ decomposed as products of two terms depending on the slice k and time frame t, respectively. The relevant data structure is a set of PET measurements of the form $\{z_{ikt}, i = 1, 2, \ldots, N; k = 1, 2, ..., K, t = 1, 2, ..., T\}$ corresponding to a collection of N phantom-voxels each recorded over T time-frames on each of K transverse slices in the field of view of the scanner.

All component parameters are non-negative and we impose the additional constraints, $\sum_t \mu_t = \sum_t \phi_t = 1$, for identifiability.

While the above formulation connects to the ROI analysis of PET-measured tissue time-course data, it is relevant to analysis of physical phantom measurements used in routine quality assurance of PET scanners. This is discussed more fully below. For analysis purposes, we regard z_{ikt} for $i = 1, 2, ..., N$ as a random sample from a $\text{Gamma}(\boldsymbol{\mu}_{kt}/\boldsymbol{\phi}_{kt}, \boldsymbol{\phi}_{kt})$ distribution in which the multiplicative constraints of equation (1) are in force. Previous reports on constructs of this type for PET images have been presented in [15, 16].

Estimation: We consider use of a Gamma likelihood for estimation of parameters in the multiplicative model associated with the $\{z_{ikt}\}$ data above. Assuming $\{z_{ikt}\}$ are independent—certainly not true in the PET imaging context but still potentially useful as a *quasi-likelihood* device for producing reasonable estimators—the scaled negative log-likelihood function is:

$$l(\boldsymbol{\mu}, \boldsymbol{\phi}) = \sum_{ikt}\{\frac{z_{ikt}}{\boldsymbol{\phi}_{kt}} - \frac{\boldsymbol{\mu}_{kt}}{\boldsymbol{\phi}_{kt}}\log(\frac{z_{ikt}}{\boldsymbol{\phi}_{kt}}) + \log(z_{ikt}) + \log(\Gamma(\frac{\boldsymbol{\mu}_{kt}}{\boldsymbol{\phi}_{kt}}))\} \tag{2}$$

where $\boldsymbol{\mu}_{kt}$ and $\boldsymbol{\phi}_{kt}$ are specified by equation (1). An alternating procedure, updating (α_k, μ_t) with (β_k, ϕ_t) fixed, followed by updating (β_k, ϕ_t) with (α_k, μ_t) fixed, is used to minimize (2). This might be viewed as a variation of the $\prod$ method of Brieman [5]. We elaborate the details of the individual steps involved in the present setting.

This article has been accepted for publication in a future issue of this journal, but has not been fully edited. Content may change prior to final publication. Citation information: DOI 10.1109/TMI.2017.2770147, IEEE Transactions on Medical Imaging

i) Updating (α_k, μ_t) *with* (β_k, ϕ_t) *fixed:* With $\boldsymbol{\gamma} = (\gamma_1, \gamma_2, ..., \gamma_T)$, for $\gamma_t = \mu_t/\phi_t$; $\boldsymbol{\theta} = (\theta_1, \theta_2, ...\theta_K)$, for $\theta_k = \alpha_k/\beta_k$ and $u_{ikt} = z_{ikt}/\phi_{kt}$. The problem becomes minimizing the following objective with respect to $(\boldsymbol{\gamma}, \boldsymbol{\theta})$

$$l(\boldsymbol{\gamma}, \boldsymbol{\theta}) = \sum_k \sum_t -\gamma_t \theta_k \log(G_{kt}) + \log(\Gamma(\gamma_t \theta_k)) \quad (3)$$

where $G_{kt} = \{\prod_i u_{ikt}\}^{1/N}$ is the geometric mean of the $\{u_{ikt}, i = 1, 2, ..., N\}$ data.
Write $\xi_{kt} = \theta_k \gamma_t$ and suppose $\xi^0_{kt} = \theta^0_k \gamma^0_t = (\alpha^0_k \mu^0_t)/(\beta^0_k \phi^0_t)$ where the super-script "0" indicates the current guess. Second order Taylor series expansion of the log-Gamma function gives

$$\begin{aligned} \log(\Gamma(\xi_{kt})) \quad &\approx \quad \log(\Gamma(\xi^0_{kt})) + \psi(\xi^0_{kt})(\xi_{kt} - \xi^0_{kt}) \\ &\quad + \frac{1}{2}\psi_1(\xi^0_{kt})(\xi_{kt} - \xi^0_{kt})^2 \quad (4) \end{aligned}$$

where ψ and ψ_1 are the di-gamma and tri-gamma functions [1]. Substitution into (3), yields a quadratic approximation to objective function used for updating $(\boldsymbol{\gamma}, \boldsymbol{\theta})$

$$\begin{aligned} WRSS(\boldsymbol{\gamma}, \boldsymbol{\theta}) \quad &= \quad \sum_k \sum_t w_{kt}(y_{kt} - \xi_{kt})^2 \\ &= \quad \sum_k \sum_t w_{kt}(y_{kt} - \theta_k \gamma_t)^2 \end{aligned}$$

where

$$y_{kt} = \xi^0_{kt} + \frac{\log(G_{kt}) - \psi(\xi^0_{kt})}{\psi_1(\xi^0_{kt})} \quad ; \quad w_{kt} = \psi_1(\xi^0_{kt})$$

This gives the updating process—given θ_k, update γ_t (normalizing so that $\sum_t \phi_t = 1$) and given γ_t, update θ_k

$$\hat{\gamma}_t \leftarrow \frac{\sum_{k=1}^K w_{kt}\theta_k y_{kt}}{\sum_{k=1}^K w_{kt}\theta_k^2} \ , \ t = 1, 2, ..., T;$$

$$\hat{\theta}_k \leftarrow \frac{\sum_{t=1}^T w_{kt}\gamma_t y_{kt}}{\sum_{t=1}^T w_{kt}\gamma_t^2} \ , \ k = 1, 2, ..., K.$$

On convergence set $\hat{\mu}_t = \hat{\gamma}_t \phi^0_t$ and $\hat{\alpha}_k = \hat{\theta}_k \beta^0_k$.

ii) Updating (β_k, ϕ_t) *with* (α_k, μ_t) *fixed:* With $\boldsymbol{\mu} = \alpha_k \mu_t$, $\boldsymbol{\zeta} = \zeta_t \omega_k$, $\zeta_t = 1/\phi_t, \omega_k = 1/\beta_k$, the objective function (2) can be expressed as

$$\begin{aligned} l(\boldsymbol{\mu}, \boldsymbol{\zeta}) \quad &= \quad \sum_{ikt} \{z_{ikt}\zeta_t\omega_k - \mu_{kt}\zeta_t\omega_k \log\left(z_{ikt}\zeta_t\omega_k\right) \\ &\quad + \log(z_{ikt}) + \log\left(\Gamma(\mu_{kt}\zeta_t\omega_k)\right)\} \quad (5) \end{aligned}$$

Now hold ω_k constant, and minimize (5) with respect to ζ_t. The relevant first and second derivatives of l are

$$\begin{aligned} g(\zeta_t) = \frac{dl}{d\zeta_t} \quad &= \quad \sum_{ik} \{z_{ikt}\omega_k - \mu_{kt}\omega_k \log\left(z_{ikt}\zeta_t\omega_k\right) \\ &\quad - \mu_{kt}\omega_k + \mu_{kt}\omega_k\psi\big(\mu_{kt}\zeta_t\omega_k\big)\} \\ h(\zeta_t) = \frac{d^2 l}{d\zeta_t^2} \quad &= \quad N \cdot \sum_k \mu_{kt}\omega_k\{\mu_{kt}\omega_k\psi_1\big(\mu_{kt}\zeta_t\omega_k\big) - 1/\zeta_t\} \end{aligned}$$

This gives the Newton updating process: $\zeta^1_t = \zeta^0_t - g(\zeta^0_t)/h(\zeta^0_t)$. On convergence, $\hat{\phi}_t = 1/\hat{\zeta}_t$ and scaled so that $\sum_t \hat{\phi}_t = 1$.

With ζ_t (equivalently ϕ_t) fixed, the Newton process for updating ω_k proceeds as: $\omega^1_k = \omega^0_k - g(\omega^0_k)/h(\omega^0_k)$ where

$$\begin{aligned} g(\omega_k) = \frac{dl}{d\omega_k} \quad &= \quad \sum_{it} \{z_{ikt}\zeta_t - \mu_{kt}\zeta_t \log\left(z_{ikt}\zeta_t\omega_k\right) \\ &\quad - \mu_{kt}\zeta_t + \mu_{kt}\zeta_t\psi\big(\mu_{kt}\zeta_t\omega_k\big)\} \\ h(\omega_k) = \frac{d^2 l}{d\omega_k^2} \quad &= \quad N \cdot \sum_t \mu_{kt}\zeta_t\{\mu_{kt}\zeta_t\psi_1\big(\mu_{kt}\zeta_t\omega_k\big) - 1/\omega_k\} \end{aligned}$$

On convergence, $\hat{\beta}_k = 1/\hat{\omega}_k$. We update μ_t, α_k and ϕ_t, β_k sequentially by iterating the procedures in section *i)* and *ii)* above. The iterative process continues until relative differences are lower than the specified tolerance.

$$\varepsilon_\mu = \left\| \frac{\mu^n_{kt} - \mu^{n-1}_{kt}}{\mu^n_{kt}} \right\| < 0.001 \ ; \ \varepsilon_\phi = \left\| \frac{\phi^n_{kt} - \phi^{n-1}_{kt}}{\phi^n_{kt}} \right\| < 0.001$$

The process is initialized in a simplified least squares (LS) way, alternating between the following two steps for μ and α—with starting values $\tilde{\mu}_t = \frac{1}{N \times K}\sum_{i=1}^N \sum_{k=1}^K z_{ikt}$

- $\tilde{\alpha}_k = \frac{\frac{1}{N}\sum_{it} z_{ikt}\tilde{\mu}_t}{\sum_t \tilde{\mu}_t^2}$
- $\tilde{\mu}_t = \frac{\frac{1}{N}\sum_{ik} z_{ikt}\tilde{\alpha}_k}{\sum_k \tilde{\alpha}_k^2}$, normalizing so that $\sum_t \tilde{\mu}_t = 1$.

This is followed by setting $y_{ikt} = (z_{ikt} - \tilde{\alpha}_k\tilde{\mu}_t)/\sqrt{\tilde{\alpha}_k\tilde{\mu}_t}$ and alternating the two steps

- $\tilde{\beta}_k = \frac{\frac{1}{N}\sum_{it} y_{ikt}^2\tilde{\phi}_t}{\sum_t \tilde{\phi}_t^2}$
- $\tilde{\phi}_t = \frac{\frac{1}{N}\sum_{ik} y_{ikt}^2\tilde{\beta}_k}{\sum_k \tilde{\beta}_k^2}$, normalizing so that $\sum_t \tilde{\phi}_t = 1$

for determining ϕ and β. In this setting, IRLS is equivalent to Newton's method and can therefore be expected to benefit from its convergence properties [14]. The process is self-consistent in the sense that if the parameters are set at the true values, any of the individual updating steps is unbiased for the target. We evaluate the efficiency of these simplified estimators in results section.

B. Probability Transformed Normalized Residuals

Let $F(\cdot|\mu, \phi)$ be the cumulative distribution for a Gamma random variable Z with density $\text{Gamma}(\mu/\phi, \phi)$. Consider the probability transformation of Z

$$R = \Phi^{-1}(F(Z|\mu, \phi))$$

where Φ^{-1} is inverse cumulative distribution function of a standard Gaussian. Theoretically, R must have a standard normal distribution—Fig. 2. If the model is correct, the probability-transformed data might be considered as realizations from a normal distribution.

In the context of the multiplicative model, where μ_{kt} and ϕ_{kt} are estimated, we can use this to construct a set of normalized model residuals for the analysis

$$r_{ikt} = \Phi^{-1}(F(z_{ikt}|\hat{\mu}_{kt}, \hat{\phi}_{kt}))$$

for $i = 1, 2, ..., N$, $k = 1, 2, ..., K$ and $t = 1, 2, ..., T$. If the model is appropriate, these residuals should conform to the assumptions of a random sample from a standard normal distribution. There is of course considerable experience with similar residual diagnostics in the context of the linear

This article has been accepted for publication in a future issue of this journal, but has not been fully edited. Content may change prior to final publication. Citation information: DOI 10.1109/TMI.2017.2770147, IEEE Transactions on Medical Imaging

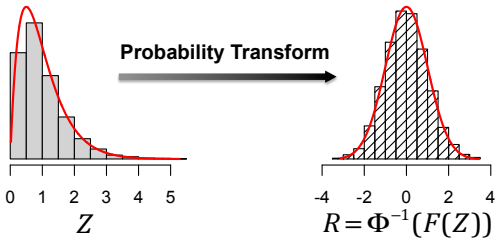

Fig. 2. Theoretical probability transformation of a Gamma random variable (Z) with distribution function F to a normal random variable R.

model—see Weisberg [25] for example. It is worth noting that as $\hat{\mu}_{kt}/\hat{\phi}_{kt}$ increases, z_{ikt} becomes Gaussian and the normalized residuals take the familiar form

$$r_{ikt} \approx \frac{z_{ikt} - \hat{\mu}_{kt}}{\sqrt{\hat{\phi}_{kt}\hat{\mu}_{kt}}} \ .$$

Thus the probability-transformed Gamma model residuals reduce to Pearson residuals as $\hat{\mu}_{kt}/\hat{\phi}_{kt}$ increases—$c.f.$ generalized linear models [14]. It should be appreciated that transformation to the normal distribution for residual diagnostics is somewhat arbitrary, a referee has suggested transforming to a uniform distribution.

III. Experimental Methods

A. Physical Phantom Data

A standard part of routine quality assurance for PET scanners involves evaluating accuracy and reliability from imaging of a known source. A range of phantoms and imaging protocols, matched to operational clinical practice, are used for this. We consider the data of this type collected at a PET imaging facility at a local hospital—the Cork University Hospital. The scanner is a GE Discovery STE used clinically for imaging of cancer patients. Routine clinical image reconstruction is performed with 3-D iterative EM reconstruction (IR). Classical linear 3-D Fourier rebinning filtered-backprojection reconstructions (FBP) are also produced. In our study, an uniform cylindrical phantom filled with F-18 radiotracer is placed in the scanner and imaged in accordance with a standard dynamic PET-FDG brain imaging protocol established by the CQIE project of the American College of Radiology Imaging Network (ACRIN) [20]. The brain imaging field of view (FOV) for PET is 700 mm trans-axially and 157 mm axially. The phantom is 215 mm in diameter and placed centrally so that its axis aligns with the long-axis of the scanner. A dynamic sequence of 45 time-frames is acquired for 55 minutes. For each time-frame, the reconstructed image has 128×128 pixels in 47 slices, with the pixel size of 5.47× 5.47 mm^2 and slice thickness of 3.27 mm. After discarding the two extreme slices, the dimension of the full 4-D phantom image data set is 128×128×45×45. The ROI data for the interior cross-sectional circular volume of the phantom, acquired for each axial slice, k, and time-frame, t, are available for analysis. There are $N = 680$ voxels in the ROI. The data for the set of all $K = 45$ slices and $T = 45$ time-frames structured as $\{z_{ikt}, i = 1, 2, ..., N, k = 1, 2, ..., K, t = 1, 2, ..., T\}$. These measurements are decay-corrected and scaled by the known dose per unit volume within the phantom. The perfect scanner would have z-values close to unity throughout. We use these data to evaluate the plausibility of the Gamma distribution versus the more conventional Gaussian assumption. We go on to use the multiplicative model to analyze the axial and temporal patterns in the bias and variance of measurements. Note that the central placement and small diameter of the phantom, makes radial effects negligible in this setting.

1) Assessment of the Gamma and Log-normal Distributions: The cross-sectional voxel-data for each time-frame and slice are evaluated for conformity to a Gaussian, Gamma and log-normal law. The Gamma and log-normal model are estimated using the function `fitdistr` in R [24]. The likelihood ratio statistic comparing twice the negative log-likelihood of the best fitting Gaussian model is compared to twice the negative log-likelihood for the best fitting Gamma model. From standard parametric likelihood theory, we would expect that if the models were equally valid the deviation of the Gamma model log-likelihood from the Gaussian log-likelihood should be on the order of a χ^2_2 random variable. To formally assess the strength of evidence in favour of the Gamma model, we compute the difference between the Gaussian log-likelihood and the Gamma model log-likelihood and evaluate the probability (p-value) that a χ^2_2 random variable could be more than the computed amount. This calculation is carried out individually for each slice and time-frame combination. A graphical comparison between the Gamma and Gaussian is also carried out. This is based on the overall structure of probability transformed residuals under Gamma and Gaussian model assumptions for the data. The likelihood ratio of the Gamma and log-normal fits are also evaluated. These are summarized by the duration of the time-frame.

2) Application of the Multiplicative Model: The model described in section II is used to evaluate the axial and temporal bias and variance. The Gamma model fit is compared to the fit achieved using the simplified least squares approach—optimal under Gaussian assumptions. In addition, the normalized residuals are analyzed and compared to the corresponding residuals obtained without the multiplicative modeling constraints.

B. Numerical Phantom Study

A numerical phantom study was conducted to explore effects of iteration and count rate on the noise distribution characteristics of EM reconstructed images. The 2-D uniform elliptical disk phantom, shown in Fig. 5, was used. The simulation model was based on simple analytical projection. One thousand replicates of Poisson simulated projection data were created with counts rates from 10^4 to 10^6 events. This lead to a collection of 1000 reconstructed images for each count rate. The central pixel value over these sets were evaluated for conformity to Gamma and log-normal distributions.

C. Numerical Simulation with the Gamma Model

Our study here investigates the performance of the method proposed in section II for estimation of the accuracy ($\boldsymbol{\mu}_{kt}$)

This article has been accepted for publication in a future issue of this journal, but has not been fully edited. Content may change prior to final publication. Citation information: DOI 10.1109/TMI.2017.2770147, IEEE Transactions on Medical Imaging

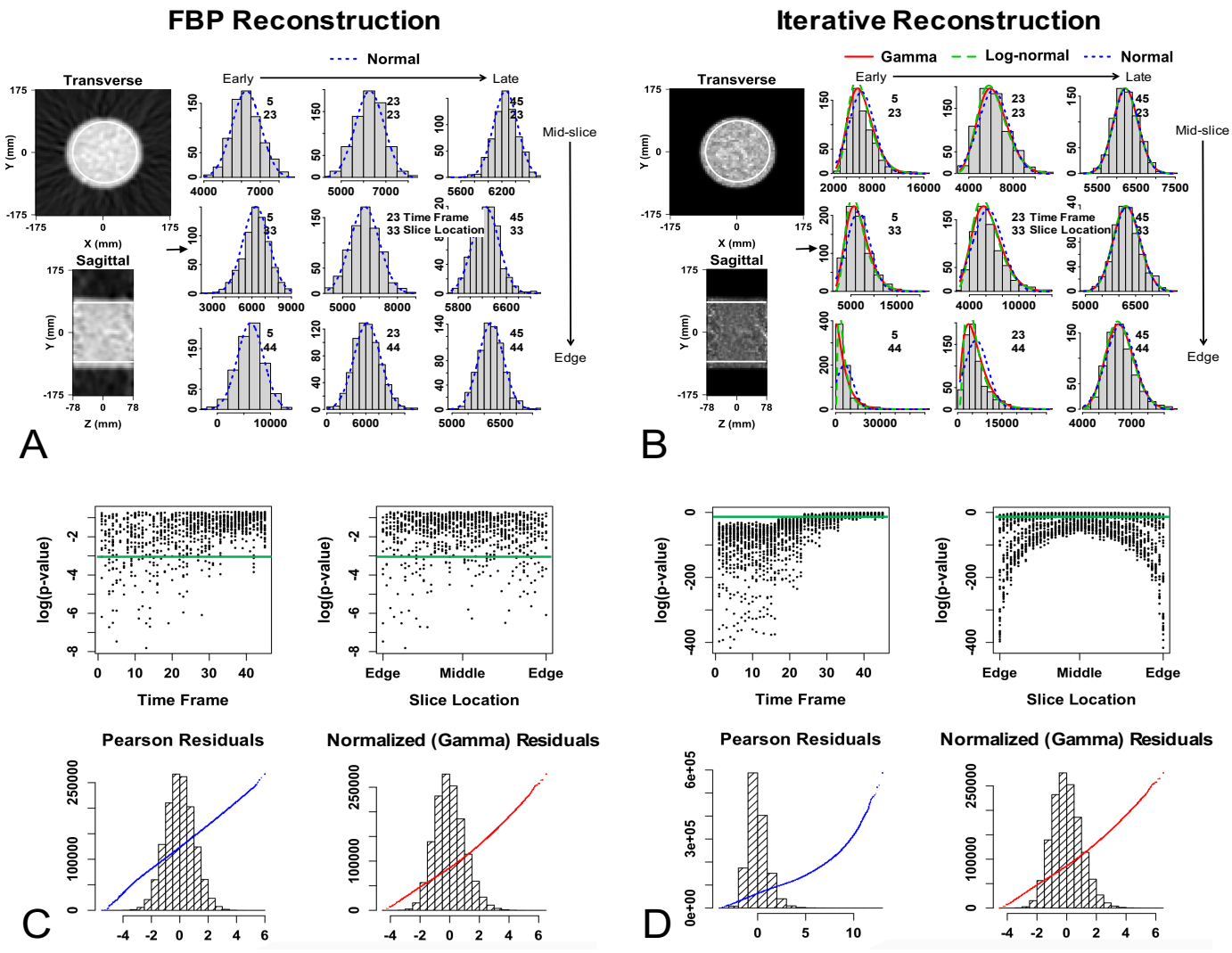

Fig. 3. 3D dynamic PET study on a cylindrical phantom using FBP (**A,C**) and EM (IR) (**B,D**) reconstructed methods. The ROI data within white outline are used in analysis. **Figure A and B:** Left: The cross-section and sagittal image of the phantom data (24th time frame of slice 23). Right: Histograms generated from ROIs on different time frames and slices. The lines on the plots are Gamma (red), log-normal (green) and normal (blue) model fits for particular time and slice combinations of ROI data. **Figure C and D:** Top: χ^2_2 p-values (log-scale) calculated for each time and slice combinations and plotted by time frame and slice location. The green lines indicate the significant level—0.05. Bottom: Histograms and normal Q-Q plots of Pearson residuals (left blue) and normalized Gamma residuals (right red) for entire phantom data.

and dispersion (ϕ_{kt}) characteristics. Data were simulated according to

$$z_{ikt} \sim \text{Gamma}(\tau \frac{\boldsymbol{\mu}_{kt}}{\boldsymbol{\phi}_{kt}}, \boldsymbol{\phi}_{kt}/\tau)$$

for $i = 1, ..., N$, $k = 1, ..., K$, and $t = 1, ..., T$, with $\boldsymbol{\mu}_{kt} = \alpha_k \mu_t$, $\boldsymbol{\phi}_{kt} = \beta_k \phi_t$ and the values of μ_t, α_k, ϕ_t and β_k, matched to typical patterns observed in the CUH phantom data. A range of dose levels τ and ROI sizes N are considered. The dose ranges are set to explore values which would be one to two orders of magnitude greater and less than that seen in the CUH sets. The ROI sizes of $N = 10, 100, 1000$ were considered. Mean square errors (MSE) for the component parameters, μ_t, α_k, ϕ_t and β_k, are evaluated as function of dose and ROI size.

IV. Results

We begin by presenting results of the analysis of physical phantom data, this is followed by numerical simulation studies.

A. Physical Phantom Data

Temporal and Spatial Data Distribution: Fig. 3 A and B shows images of slice 23 and time frame 24 located near the center of the phantom, which are reconstructed using FBP and IR methods, respectively. Voxel-level data in a cylindrical volume, within white outline, are used in analysis. The ROI histograms with the best fitting normal model (blue dotted lines), Gamma model (red lines) and log-normal model (green dashed lines) for the data in different slices and time frames are also exhibited in Fig. 3 A and B. In the present study, the FBP images show no skewness supporting the Gaussian

This article has been accepted for publication in a future issue of this journal, but has not been fully edited. Content may change prior to final publication. Citation information: DOI 10.1109/TMI.2017.2770147, IEEE Transactions on Medical Imaging

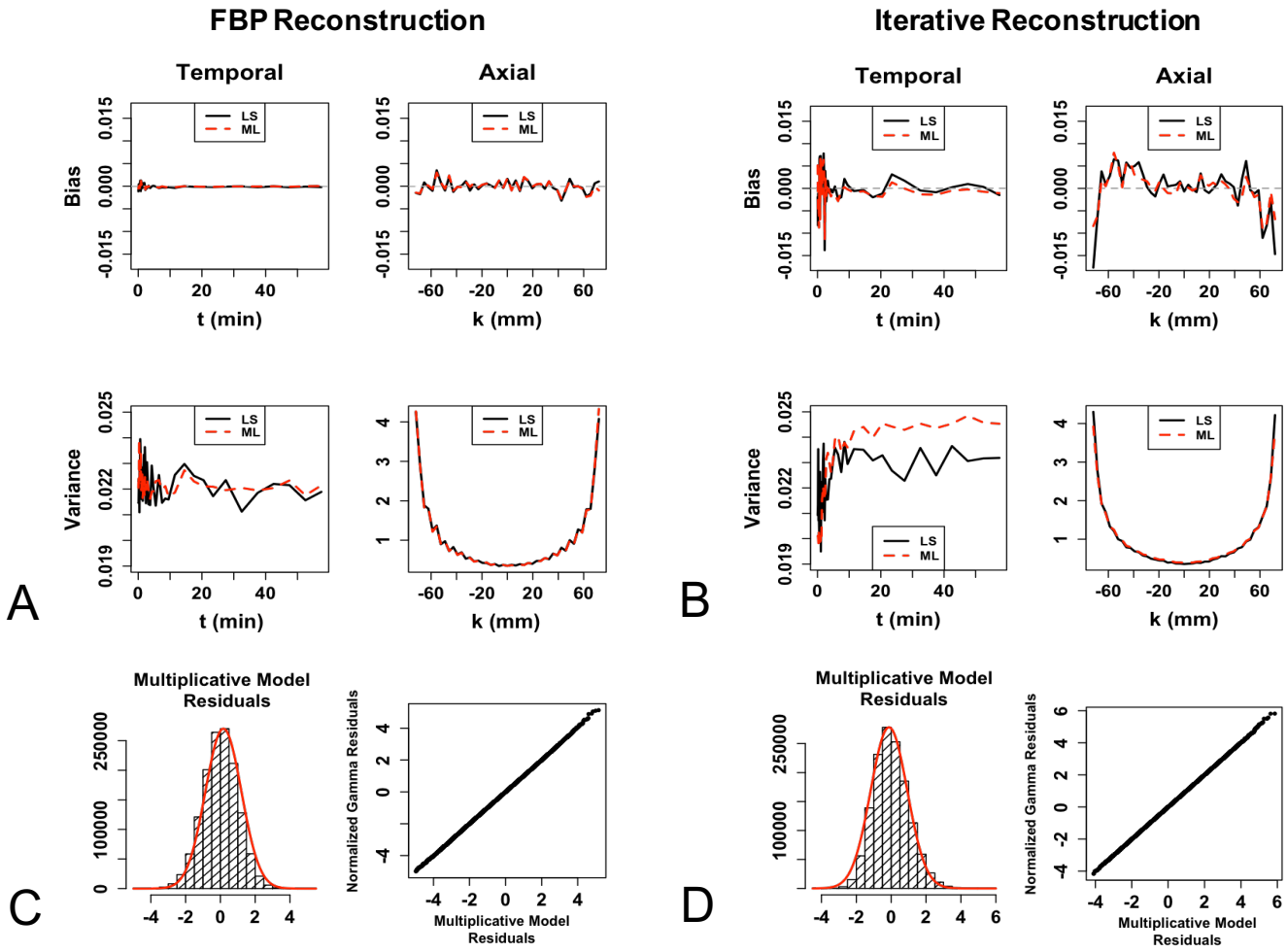

Fig. 4. Multiplicative model fit on FBP (**A,C**) and EM (iterative) (**B,D**) reconstructed PET images. **Figure A and B:** Multiplicative model estimates of bias and variance using Least Square (LS) versus Maximum Likelihood (ML) estimation. **Figure C and D:** show multiplicative model residuals and the Q-Q plot of normalized Gamma residuals with and without the multiplicative constraint.

distribution consistent with previous studies [22]. By contrast, the IR images show skewness particularly in the early time frames (Fig. 3 B) and towards the axial limits (edge) of the scanner. However, for images in late time frames and towards the middle of the scanner the skewness disappears and there is convergence to the normal distribution. The red lines in this plot indicate that the IR images can be approximated by the Gamma model, while the blue dashed lines show that the normal model fails to describe the IR images in early time frames. The log-normal model appears similar to the Gamma model for most slices. The detailed analysis of discrimination between the log-normal and Gamma model will be presented in section V. Since the measurable count rate (τ) diminishes with decay (time) and sensitivity (axial extremity), the data shown in Fig. 3 agree with the structure of $\text{Gamma}(\tau\frac{\mu}{\phi}, \phi/\tau)$ distribution—showing less skewness as τ increases (see Fig. 1).

Comparison of Gaussian and Gamma model: The top row of Fig. 3 C and D, plots χ^2_2 p-values (p_{kt}) by slice location (k) and time frame (t). This calculation has been described in section III-A1. For FBP images, the majority of p-values are in the range of 0.05 to 1 and there is no obvious temporal or axial pattern. Overall there is no significant difference between the Gaussian model fit and Gamma model fit for FBP images. With the IR images, there is strong evidence against the Gaussian model at early time frames and in extreme axial slices. These areas have less counts and show more skewness. The probability transformations of FBP and IR images are shown on the bottom row of Fig. 3 C and D, respectively. The plots on the left showing the histograms and normal quantile-quantile (Q-Q) plots of Pearson residuals $r^G_{ikt} = (z_{ikt} - \mu^*_{kt})/\sigma^*_{kt}$, where μ^*_{kt} and σ^*_{kt} are the means and variances of each slice and time-frame combination. On the bottom right of Fig. 3 C and D shown the histograms and normal Q-Q plots of normalized Gamma residuals $r^\Gamma_{ikt} = \Phi^{-1}(F(z_{ikt}|\hat{\mu}^*_{kt}, \hat{\phi}^*_{kt}))$, where $\hat{\mu}^*_{kt}$ and $\hat{\phi}^*_{kt}$ are obtained by fitting Gamma distribution for each slice and time-frame combination using `fitdistr` function in R. Both Pearson and Gamma residuals of FBP images appear Gaussian, suggesting that either model is reasonable. However the Gamma residuals of IR images are

This article has been accepted for publication in a future issue of this journal, but has not been fully edited. Content may change prior to final publication. Citation information: DOI 10.1109/TMI.2017.2770147, IEEE Transactions on Medical Imaging

strongly Gaussian in comparison to the Pearson residuals, favoring the Gamma model. To sum up, the Gamma model is superior to the Gaussian for iterative reconstruction PET images, but both models are equivalent for FBP reconstruction images.

Evaluation of Temporal and Spatial Scanning Characteristics: The maximum likelihood (ML) estimation, described in section II, is used to evaluate the axial and temporal bias and variance. The ML fit is compared to the fit achieved using the least squares (LS) approach. Note LS estimates are used as initial values for the ML computation. The estimated bias and variance using LS and ML method are shown in Fig. 4 A and B, respectively. For FBP reconstruction, the bias remains stable and stays near zero temporally and axially while the variance shows more fluctuations at the early time. In the case of IR reconstruction, the bias and variance show more fluctuations than in FBP. The variance shows some increase over time. Both FBP and IR images show a strong axial pattern of variance—low variance in the center of the scanner and high variance towards axial edge. There is no significant difference between LS and ML estimates for FBP images, but the ML estimates for IR images tend to fluctuate less than the LS estimates. Since the true variances are unknown, it is not possible to compare the accuracy of two estimates here, however our simulation study, which is reported in IV-C below, would suggest the ML estimation should be more reliable. Fig. 4 C and D show the probability transformation (multiplicative model residuals) and Q-Q plot of normalized Gamma residuals with and without the multiplicative constraint. The linear patterns of Q-Q plots suggest that the distribution of multiplicative model residuals r_{ikt} (with the constraint) and normalized Gamma residuals r^{Γ}_{ikt} (without the constraint) are similar.

B. Numerical Phantom Simulation

Phantom data results are shown in Fig. 5. Higher skewness is seen at the lower counts. The red solid lines in Fig. 5 represent fits of Gamma distributions to the measured data. The fits are very reasonable. The log-normal shows similar fits to the data (green broken lines). Fig. 5 demonstrates that the distribution of the measured data becomes closer to the normal distribution as count rate increases. The result suggests that measured data becomes closer to the normal distribution as count rate increases, in agreement with analysis of physical phantom data.

C. Numerical Simulation with the Gamma Model

The simulated data were generated as described in section III-C. The top row of Fig. 6 shows the overall histogram of Pearson residuals r^{G}_{ikt} for 3 different values of τ for a simulated dataset ($N = 1000$). The Pearson residuals become more Gaussian distributed as τ increases. This result agrees with the property of Gamma distribution as shown in Fig. 1. The bottom row shows the Gamma model residuals r_{ikt} for the same dataset. The Gamma-transformed residuals are strongly Gaussian in comparison to the Pearson residuals.

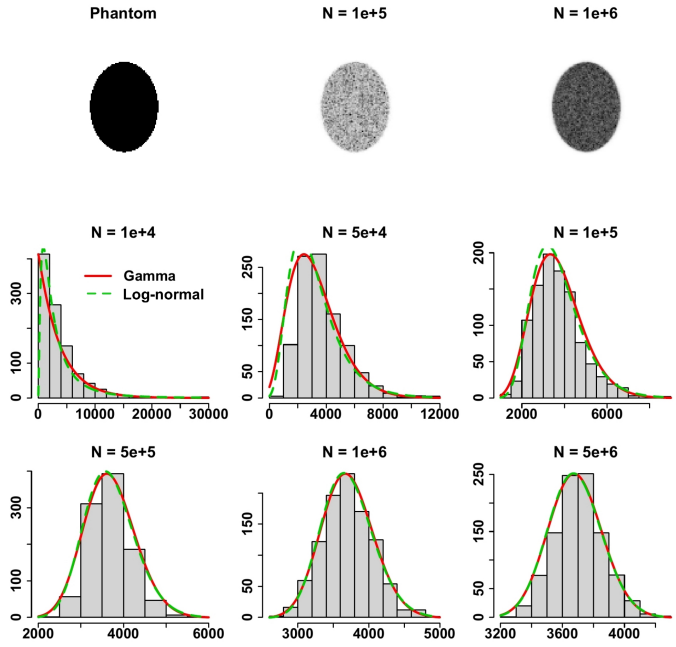

Fig. 5. Results of numerical phantom simulation study. Top: Phantom image and EM reconstructed images for two count rates ($N = 10^5$ and $N = 10^6$). Middle and bottom: Histograms of pixel values for different count rates. The Gamma and log-normal model fits are shown in red and green, respectively.

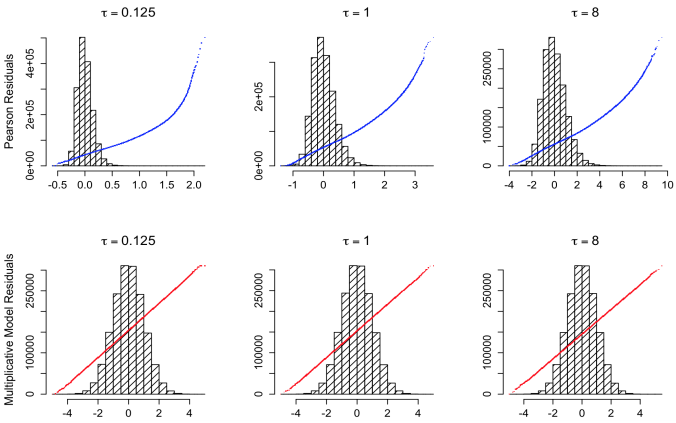

Fig. 6. Histograms and normal Q-Q plots (dots) of the Pearson (top) and Gamma-transformed residuals (bottom) for different τ values.

Considering the data with same dose $\tau = 1$, Fig. 7 compares the initial least squares estimates (blue)—$\tilde{\mu}_t$, $\tilde{\alpha}_k$, $\tilde{\phi}_t$, $\tilde{\beta}_k$ with the multiplicative model/maximum likelihood estimates (red)—$\hat{\mu}_t$, $\hat{\alpha}_k$, $\hat{\phi}_t$, $\hat{\beta}_k$. The ML estimates follow the true values more closely indicating that the Gamma distribution-based multiplicative model improves the accuracy of estimation.

Fig. 8 shows the log mean square error (MSE) of the component ML (red) and LS (blue) parameter estimation evaluated as a function of the dose τ and ROI size N. The results indicate that compared to LS, ML estimates have reduced MSEs. The amount of reduction depends on τ, N and the parameter being estimated. The percentage reductions of MSE for μ_t and α_k are 2% and 78%, respectively, with $\tau = 1$ and $N = 1000$—these values match the physical phantom

This article has been accepted for publication in a future issue of this journal, but has not been fully edited. Content may change prior to final publication. Citation information: DOI 10.1109/TMI.2017.2770147, IEEE Transactions on Medical Imaging

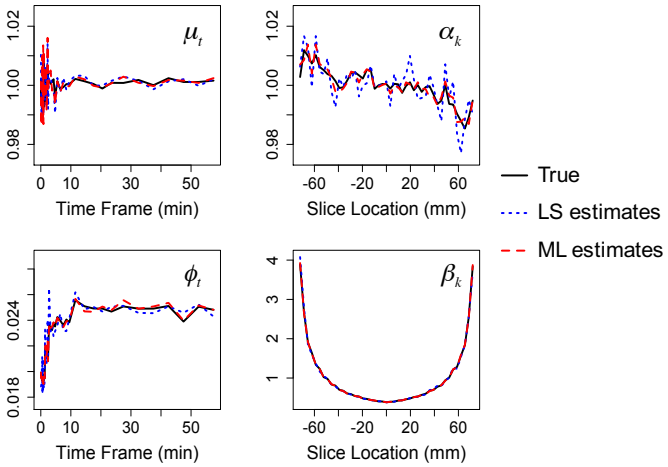

Fig. 7. Initial (LS) and multiplicative (ML) estimates for μ_t, α_k, ϕ_t and β_k when $\tau = 1$.

data. The MSE reduction of ϕ_t and β_k are higher, 96% and 95%. The compute time for ML is about four times that of the LS estimation method—for a sample size of $N = 1000$ the total compute time was 111 seconds on a laptop with a 2.9 GHz processor. The results also show that the estimation is consistent as τ and N increase. The empirical rate of convergence of the MSE of the mean value parameters μ_t and α_k, was analyzed by linear regression using the model, $\log(MSE) \sim a_0 + a_1 \log(N) + a_2 \log(\tau)$. The regression lines are shown on the plot. The estimated regression coefficients $\hat{a}_0$, $\hat{a}_1$ and $\hat{a}_2$ of the log MSE of the ML estimation of μ_t and α_k are presented in Table I. The empirical behaviour MSE of ML estimation for ϕ_t, β_k shows a rate change close to $\tau = 1$. After $\tau = 1$ the MSE shows little improvement with increasing τ. In light of this regression separate lines were fitted for $\tau \leq 1$ and $\tau \geq 1$, respectively. The estimated regression coefficients are given in Table II. An asymptotic explanation of the behaviour is offered in the next section.

TABLE I
EMPIRICAL MSE ESTIMATION CHARACTERISTIC FOR μ_t AND α_k
$\log(\text{MSE}) \sim a_0 + a_1 \log(N) + a_2 \log(\tau)$

	μ_t	α_k
$\hat{a}_0$	-4.727 ± 0.243	-5.969 ± 0.172
$\hat{a}_1$	-0.818 ± 0.049	-0.893 ± 0.035
$\hat{a}_2$	-1.311 ± 0.066	-1.135 ± 0.047

TABLE II
EMPIRICAL MSE ESTIMATION CHARACTERISTIC FOR ϕ_t AND β_k
$\log(\text{MSE}) \sim a_0 + a_1 \log(N) + a_2 \log(\tau)$

		ϕ_t	β_k
$\tau \leq 1$	$\hat{a}_0$	-3.685 ± 0.278	-3.578 ± 0.420
	$\hat{a}_1$	-0.579 ± 0.050	-0.755 ± 0.075
	$\hat{a}_2$	-1.004 ± 0.121	-0.686 ± 0.183
$\tau \geq 1$	$\hat{a}_0$	-3.359 ± 0.434	-2.449 ± 0.185
	$\hat{a}_1$	-0.625 ± 0.064	-1.013 ± 0.027
	$\hat{a}_2$	-0.127 ± 0.213	-0.067 ± 0.091

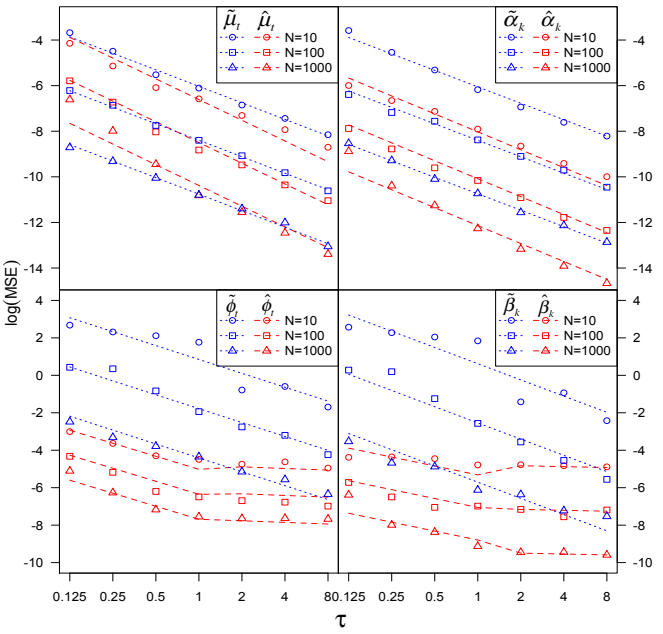

Fig. 8. The log MSE of the parameter estimation evaluated as function of dose τ and ROI size N. The log MSE for initial (LS) estimates are shown in blue and multiplicative model (ML) estimates are shown in red.

V. Discussion

Using quantile-quantile (Q-Q) plots and less formal statistical methods, Teymurazyan et al. [22] showed that the noise in RAMLA-reconstructed PET images was well characterized by the Gamma distribution while FBP reconstructions produced comparable conformity with both normal and Gamma statistics. This study uses a more formal likelihood based approach to investigate evidence in support of the Gamma model in the EM and FBP reconstructed images. The test method is applied to QA data from a phantom study obtained from a PET scanner in routine clinical use. The analysis shows strong evidence in support of the Gamma-model representation of EM reconstructed images. FBP reconstructed images are adequately described by Gaussian distributions. On the basis of these results, we have described an approach for improved statistical analysis of PET images that has been reconstructed using practically used iterative (EM) methods. It involves a novel use of IRLS for implementation of a Gamma-based likelihood. Our experience with various data sets shows that the algorithm is always converged after a modest number of iterations. The approach also involves consideration of probability transformed residuals for diagnostic analysis. The approach is developed in the context of multiplication spatial-temporal models used in QA of PET scanners. The method is applied to estimate the bias and variance in QA data from a phantom study obtained from a PET scanner in routine clinical use.

A. Theoretical Interpretation of MSE Characteristics

The simulation results presented describe the Gamma-model MSE characteristics for the class of multiplicative spatial-temporal models used in QA evaluation of PET scanners.

This article has been accepted for publication in a future issue of this journal, but has not been fully edited. Content may change prior to final publication. Citation information: DOI 10.1109/TMI.2017.2770147, IEEE Transactions on Medical Imaging

Potential benefits in efficiency are found by use of the Gamma-likelihood approach, when the data are Gamma in nature. A simplified analysis of this setup allows the measured empirical behaviour of the MSE as a function of dose and ROI size to be interpreted theoretically—see Fig. 8. Consider $\{z_1, z_2, ..., z_N\}$ a random sample of size N from a $\text{Gamma}(\tau\mu/\phi, \phi/\tau)$ distribution. For τ large, the Gamma distribution is well approximated by a Gaussian with mean μ and variance $\mu\phi/\tau$. In this limit, the maximum likelihood estimator (MLE) for μ is the sample mean

$$\hat{\mu} = \frac{1}{N}\sum_{i=1}^{N} z_i.$$

The expected MSE of this (approximate ML) estimator is

$$E(\text{MSE}(\hat{\mu})) = \frac{\text{Var}(z_i)}{N} = \frac{\mu\phi}{N\tau}$$

Hence $\log(MSE) \sim a_0 + a_1\log(N) + a_2\log(\tau)$ where $a_1 = -1$ and $a_2 = -1$. This captures the empirical behaviour of the MSE of μ and α as a function of τ and N found in the numerical simulations—see Table I.

The analysis of the error characteristics in ϕ and β in the QA multiplicative model can be examined by consideration of MLE for ϕ in the simplified setup. Here analysis is made easier if we suppose μ is known. If μ is known, the (MLE) of ϕ is

$$\hat{\phi} = \frac{1}{N}\sum_{i=1}^{N} \frac{(z_i - \mu)^2}{\mu/\tau}.$$

Using the approximate χ^2_1 distribution for $[z_i - \mu]^2/(\mu\phi/\tau)$—because z_i is approximately Gaussian—the expected MSE of $\hat{\phi}$ is

$$E(\text{MSE}(\hat{\phi})) = \frac{\text{Var}([z_i - \mu]^2)}{\tau^2\mu^2 N} \approx \frac{2\mu^2\phi^2/\tau^2}{\mu^2 N/\tau^2} = \frac{2\phi^2}{N}.$$

This analysis predicts that the asymptotic MSE of $\hat{\phi}$ or $\hat{\beta}$ will not diminish with increasing τ, but it will reduce with increasing ROI size (N). So $\log(MSE) \sim a_0 + a_1\log(N) + a_2\log(\tau)$ where $a_1 = -1$ and $a_2 = 0$. While Fig. 8 does not agree with this analysis—there is an apparent non-linearity in the dependence of the $\log(MSE)$ as a function of dose (τ), the characteristic becomes remarkably flat for large dose. Table II presents estimated coefficients at large doses. These are in good agreement with the theoretical analysis.

B. Discriminating Between the log-normal and Gamma Distributions

As well known, both the log-normal and Gamma distributions may be used to describe skewed non-negative data. Kundu and Manglick [11] propose to discriminate between these two distributions using the ratio of the maximized likelihoods. Applying this procedure to our physical phantom data, we used likelihood to fit both the log-normal and Gamma model to the cross-sectional voxel data for each combination of time frame t and slice k and then calculate the ratio of the maximized likelihoods for Gamma and log-normal models. If the ratio is greater than 1, the Gamma model would be preferred, otherwise, the log-normal model is preferred. For the non-Gaussian cross-sectional data (cf. IV-A) there are 79.77% of ratio values are greater than one, which means the Gamma model is generally found more appropriate than the log-normal model in these data. Fig. 9 (left) shows box-plots of the ratio distribution across the three levels of the time frames. At the early short duration time frames (less than 30 seconds), all the ratios are greater than 1, showing very strong evidence supporting the Gamma model over the log-normal model. The evidence gets weaker with longer duration time-frames (between 30 and 1 minute) and diminished at the longest duration late time frames (more than 1 minute duration). In addition, the numerical simulation study, shown in Fig. 9 (right), agrees with this result that the Gamma model is preferable at lower count. Barrett et al. [3] provided a theoretical argument indicating how the reconstructed images might be approximated by the log-normal distribution. This was based on the assumption that the noise in the reconstructed images is relatively small—*i.e.* high-count settings. The analysis here indicates that especially in the shorter duration (lower count) time frames (the other end of the spectrum), the Gamma model is more plausible—Fig. 9.

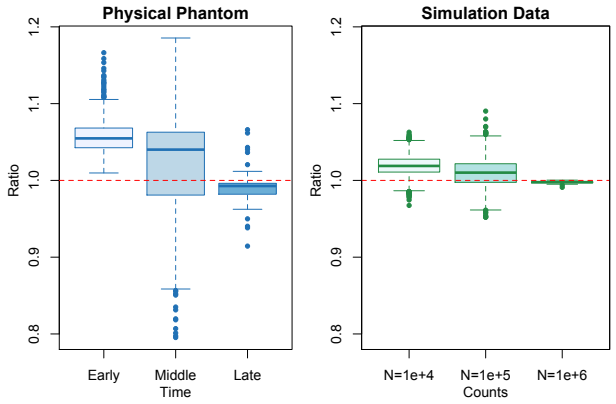

Fig. 9. The likelihood ratio of Gamma model compare to log-normal. Choose the Gamma distribution if the value is greater than 1, otherwise the log-normal distribution is preferred.

C. Impact of Spatial Covariance

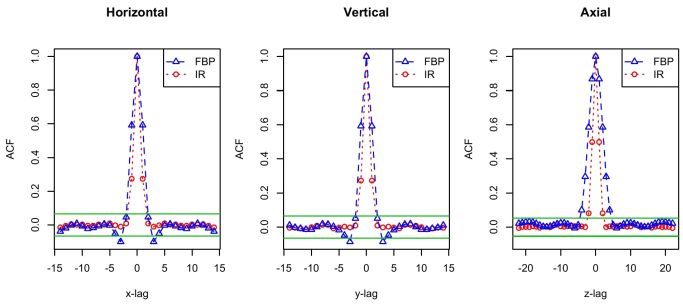

Fig. 10. One dimensional profiles of 3-D ACF of FBP and IR reconstruction physical phantom images through the center of the phantom, showing from left to right, horizontal, vertical and axial profile.

This article has been accepted for publication in a future issue of this journal, but has not been fully edited. Content may change prior to final publication. Citation information: DOI 10.1109/TMI.2017.2770147, IEEE Transactions on Medical Imaging

The analysis presented does not take account of the covariance characteristics of reconstructed PET images. In practice this is clearly important. The MSE behaviour of the Gamma-based estimation technique relative to LS could well be impacted by covariance in the ROI data. To investigate this, we adapted our simulation study to take account of the type of covariance seen in the physical phantom data. The auto-covariance used was matched to our physical phantom data by considering a hyper-rectangular volume placed inside the physical phantom (III-A) and extracting the normalized Gamma-transformed residuals $\{r_{ijk}, i = 1, 2, \ldots, I; j = 1, 2, \ldots, J; k = 1, 2, ..., K\}$.

Following the Wiener-Khinchine theorem [4], the 3-D autocorrelation function (ACF) was estimated as the inverse FFT of the 3-D power spectrum of hyper-rectangular volume data. Very similar 3-D autocorrelation patterns are observed across time frames (not shown). This is expected since time-frames are independent and the resolution filter bandwidth is not varied with frame duration. We averaged the ACF's across time-frames to produce a final 3-D ACF function. One dimensional ACF profiles through the center of the hyper-rectangular volume are shown in Fig. 10. Horizontal profiles (left) look almost same as the vertical ones (middle), indicating isotropic correlation behaviour within each slice for both FBP and EM images. There is stronger correlation in the FBP images compared to the EM images. This is no doubt due to the different mechanisms affecting the smoothness of the two data sets—the correlation is affected by the filter cut-off frequency for the FBP images [26] and, in addition, by the iteration number for the EM images [27].

We note that the simulation method in III-C generates non-correlated data. To investigate the effects of correlation on estimation accuracy of μ_{kt} and ϕ_{kt}, we modify the simulation method in III-C to simulate the PET images with 3-D autocorrelation matched to the one observed in the EM data for each time frame and slice. To simulate data, we first create T independent realisations $\{\epsilon_{ijkt}$ for $i = 1, ..., I; j = 1, 2, ..., J; k = 1, 2, ..., K$ and $t = 1, 2, ..., T\}$ of a Gaussian process with 3-D autocorrelation structure matching the spatial ACF of the phantom data. Each realisation is then transformed to produce a realisation of a Gamma process with a desired specified mean and variance pattern

$$z_{ijkt} = F^{-1}(\Phi(\epsilon_{ijkt})|\mu_{ijkt}, \phi_{ijkt})$$

where

$$\mu_{ijkt} = \alpha_k \mu_t \text{ and } \phi_{ijkt} = \beta_k \phi_t$$

Note the z_{ijkt} data has a Gamma distribution and a covariance pattern matched to the PET phantom data.

Fig. 11 shows comparison of μ_t, α_k, ϕ_t and β_k estimation based on simulated data with (blue) and without (red) 3-D autocorrelation structure. Although less accurate, estimates based on the auto-correlated data follow the true values well. The log MSE of the two estimations evaluated as a function of dose τ and ROI size N are presented in Fig. 12. $N = I \times J$. The regression model of MSE is $\log(MSE) \sim a_0 + a_1 \log(N) + a_2 \log(\tau)$—same as Fig. 8. Fig. 12 shows that the MSE of auto-correlated data behaves

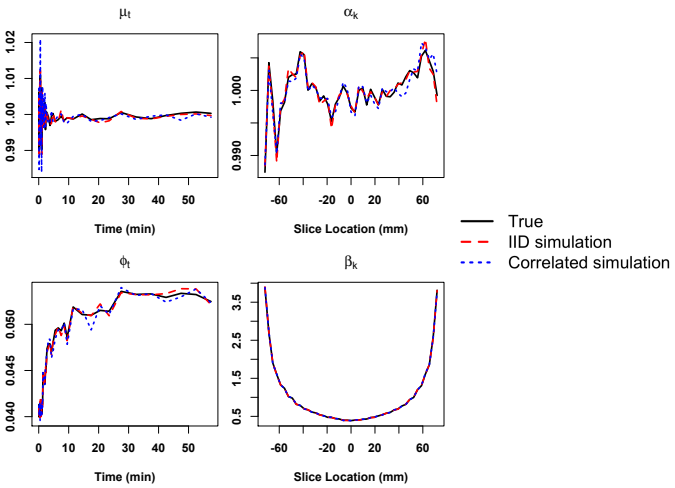

Fig. 11. Parameter estimation for $i.i.d.$ simulation versus correlated simulation.

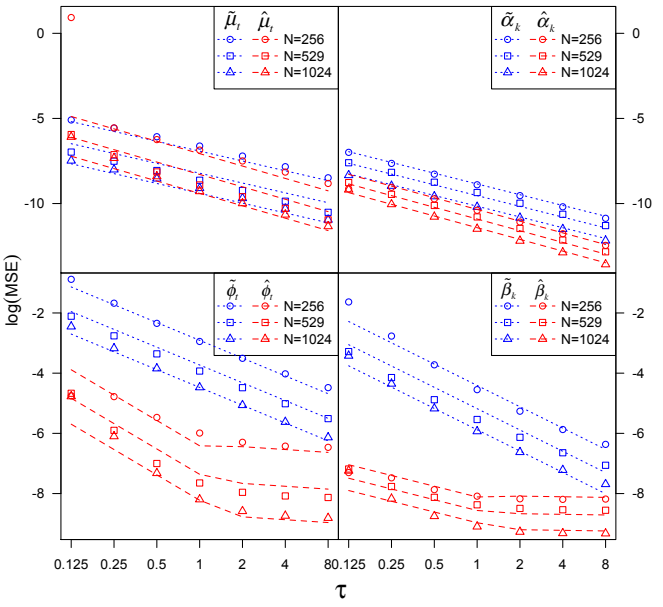

Fig. 12. The log MSE of the parameter estimation for auto-correlated data evaluated as a function of dose τ and ROI size N. The log MSE for initial (LS) estimates are shown in blue and multiplicative model (ML) estimates are shown in red.

similar to the non-correlated data (compare to Fig. 8). The MSE is consistent as τ increases as well as N increases. The ML algorithm significantly reduces the MSE compare to LS. The ML algorithm is under the assumption of $i.i.d.$ data, it is not optimal for correlated data, however, the ML estimation is still acceptable and the MSE behavior follows the theoretical interpretation discussed in section V-A.

D. Generalizability to other PET Scanners

We have evaluated a collection of 34 phantom data sets collected by the ACRIN on PET scanners that use positivity

This article has been accepted for publication in a future issue of this journal, but has not been fully edited. Content may change prior to final publication. Citation information: DOI 10.1109/TMI.2017.2770147, IEEE Transactions on Medical Imaging

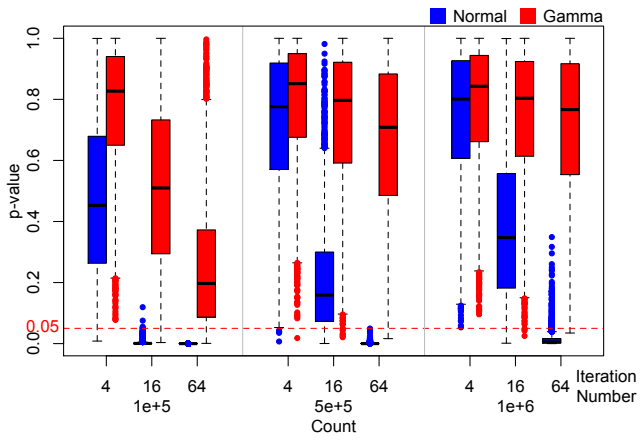

Fig. 13. The Kolmogorov-Smirnov test p-values of Gamma and normal model for numerical phantom simulation data with different iteration numbers (4, 16, 64) and counts (1e+5, 5e+5, 1e+6).

constrained reconstructions. These data sets are reconstructed using different iterative methods, such as RAMLA, OSEM and True-X. Our analysis, which will be reported separately, finds strong support for the Gamma distribution. In light of this we anticipate that there is potential to use the Gamma model to generally describe the behaviour positively constrained PET scanner data.

E. Concluding Remarks

Overall the work shows that statistical adaptation to the Gamma-structure of iteratively reconstructed PET images is readily achieved. This has the potential to enhance the statistical efficiency of inferences obtained from such data. As shown in Fig. 13, in our Numerical Phantom Study simulation setting the Gamma model is superior to normal model especially at higher iteration numbers and lower counts. The data is more skewed as iteration number increases so that the Gamma model fit is better compared to normal. The probability transformed Gamma residuals provide a very useful diagnostic in this context. Refinement of these techniques to provide a full treatment of the distribution of PET scanner data in 3-D, including the covariance patterns, is clearly of interest. The model above is a starting point for that development. Investigation of that approach is currently underway and will be reported in future work.

REFERENCES

[1] M. Abramowitz and I. A. Stegun, *Handbook of mathematical functions: with formulas, graphs, and mathematical tables*. Courier Corporation, 1964, vol. 55.

[2] N. Alpert, D. Chesler, J. Correia, R. Ackerman, J. Chang, S. Finklestein, S. Davis, G. Brownell, and J. Taveras, "Estimation of the local statistical noise in emission computed tomography," *IEEE transactions on medical imaging*, vol. 1, no. 2, pp. 142–146, 1982.

[3] H. H. Barrett, D. W. Wilson, and B. M. Tsui, "Noise properties of the EM algorithm. I. Theory," *Physics in medicine and biology*, vol. 39, no. 5, pp. 833–846, 1994.

[4] G. E. Box, G. M. Jenkins, G. C. Reinsel, and G. M. Ljung, *Time series analysis: forecasting and control*. John Wiley & Sons, 2015.

[5] L. Breiman, "The Π method for estimating multivariate functions from noisy data," *Technometrics*, vol. 33, no. 2, pp. 125–143, May 1991.

[6] R. E. Carson, Y. Yan, M. E. Daube-Witherspoon, N. Freedman, S. L. Bacharach, and P. Herscovitch, "An approximation formula for the variance of PET region-of-interest values," *IEEE transactions on medical imaging*, vol. 12, no. 2, pp. 240–250, Jun. 1993.

[7] R. Huesman, "The effects of a finite number of projection angles and finite lateral sampling of projections on the propagation of statistical errors in transverse section reconstruction," *Physics in Medicine and Biology*, vol. 22, no. 3, pp. 511–521, 1977.

[8] R. H. Huesman, "A new fast algorithm for the evaluation of regions of interest and statistical uncertainty in computed tomography," *Physics in Medicine and Biology*, vol. 29, no. 5, pp. 543–552, 1984.

[9] M. Ibaraki, K. Matsubara, K. Nakamura, H. Yamaguchi, and T. Kinoshita, "Bootstrap methods for estimating PET image noise: experimental validation and an application to evaluation of image reconstruction algorithms," *Annals of nuclear medicine*, vol. 28, no. 2, pp. 172–182, Feb. 2014.

[10] P. E. Kinahan and J. W. Fletcher, "Positron emission tomography-computed tomography standardized uptake values in clinical practice and assessing response to therapy," in *Seminars in Ultrasound, CT and MRI*, vol. 31, no. 6. Elsevier, Dec. 2010, pp. 496–505.

[11] D. Kundu and A. Manglick, "Discriminating between the log-normal and gamma distributions," *Journal of the Applied Statistical Sciences*, vol. 14, pp. 175–187, 2005.

[12] Y. Li, "Noise propagation for iterative penalized-likelihood image reconstruction based on Fisher information," *Physics in medicine and biology*, vol. 56, no. 4, pp. 1083–1103, 2011. [Online]. Available: http://stacks.iop.org/0031-9155/56/i=4/a=013

[13] R. Maitra and F. O'sullivan, "Variability assessment in positron emission tomography and related generalized deconvolution models," *Journal of the American Statistical Association*, vol. 93, no. 444, pp. 1340–1355, Dec. 1998.

[14] P. McCullagh and J. A. Nelder, *Generalized Linear Models*, 2nd ed. London, UK: CRC Press, 1989.

[15] T. Mou, J. Huang, Y. Zhang, B. Elston, P. Kinahan, M. Muzi, A. Opanowski, and F. O'Sullivan, "Spatial covariance characteristics in a collection of 3-D PET scanners used in clinical imaging trials," in *Nuclear Science Symposium and Medical Imaging Conference (NSS/MIC), 2014 IEEE*. Seattle, WA USA: IEEE, Nov. 2014, pp. M10–22.

[16] T. Mou, J. Huang, Y. Zhang, P. Kinahan, and F. O'Sullivan, "An improved statistical approach to the estimation of spatial bias and variability in reconstructed PET data," in *2015 IEEE Nuclear Science Symposium and Medical Imaging Conference (NSS/MIC)*, San Diego, CA 92108, USA, Oct. 2015, pp. 1–3.

[17] M. Normandin, R. Koeppe, and E. Morris, "Selection of weighting factors for quantification of PET radioligand binding using simplified reference tissue models with noisy input functions," *Physics in medicine and biology*, vol. 57, no. 3, pp. 609–629, 2012.

[18] C. R. Rao, *Linear statistical inference and its applications*. New York, NY, USA: John Wiley & Sons, 1973.

[19] R. W. Rowe and S. Dai, "A pseudo-Poisson noise model for simulation of positron emission tomographic projection data," *Medical physics*, vol. 19, no. 4, pp. 1113–1119, 1992.

[20] J. Scheuermann, A. Opanowski, J. Maffei, D. H. Thibeault, J. Karp, B. Siegel, M. Rosen, and P. Kinahan, "Qualification of NCI-designated comprehensive cancer centers for quantitative PET/CT imaging in clinical trials," *Journal of Nuclear Medicine*, vol. 54, no. supplement 2, pp. 334–334, 2013.

[21] E. Tanaka and H. Murayama, "Properties of statistical noise in positron emission tomography," in *International Workshop on Physics and Engineering in Medical Imaging*. International Society for Optics and Photonics, 1982, pp. 158–164.

[22] A. Teymurazyan, T. Riauka, H.-S. Jans, and D. Robinson, "Properties of noise in positron emission tomography images reconstructed with filtered-backprojection and row-action maximum likelihood algorithm," *Journal of digital imaging*, vol. 26, no. 3, pp. 447–456, 2013.

[23] Y. Vardi, L. Shepp, and L. Kaufman, "A statistical model for positron emission tomography," *Journal of the American statistical Association*, vol. 80, no. 389, pp. 8–20, 1985.

[24] W. N. Venables and B. D. Ripley, *Modern applied statistics with S-PLUS*. Springer Science & Business Media, 2013. [Online]. Available: http://www.stats.ox.ac.uk/pub/MASS4

[25] S. Weisberg, *Applied linear regression*. New York, NY, USA: John Wiley & Sons, 1985.

[26] D. W. Wilson, B. M. W. Tsui, and J. A. Terry, "Non-stationary noise characteristics for SPECT images," in *Conference Record of the 1991 IEEE Nuclear Science Symposium and Medical Imaging Conference*, vol. 3, Nov 1991, pp. 1736–1740.

[27] D. W. Wilson, B. M. Tsui, and H. H. Barrett, "Noise properties of the EM algorithm. II. Monte Carlo simulations," *Physics in medicine and biology*, vol. 39, no. 5, p. 847, 1994.